PROCEEDINGS OF SCIENCE

Distance of optically obscured evolved stars

Sandra Etoka[a,*] **and Dieter Engels**[b]

[a] *JBCA, University of Manchester,*
M13 9PL, Manchester, UK
[b] *Hamburger Sternwarte, Universität Hamburg,*
Gojenbergsweg 112, 21029 Hamburg, Germany

E-mail: `Sandra.Etoka@googlemail.com`

As intermediate-mass stars, precursors of planetary nebulae, head towards their final fate, they pass through the red-giant stage where they experience an increase of mass loss. This induces the creation of a circumstellar envelope of dust and gas. By the very end of this evolutionary stage, for those objects exhibiting the highest mass-loss rate, the amount of dust in the circumstellar envelope is such that it blocks optical radiation, turning them into so-called OH/IR stars. These stars are commonly observed throughout the Galaxy and are also observed in the Magellanic Clouds. Since optically obscured, the measurement of their distances using optical parallaxes as e.g. delivered by Gaia, is not possible. This issue can be circumvented thanks to maser emission. As their name gives it away, the physical conditions turn out to be ideal for a strong (1612-MHz) OH maser emission to be produced in the outer layers of the radially-expanding spherical circumstellar envelope. Combining single-dish monitoring and interferometric mapping of this OH maser emission, the “phase-lag” method provides a way to measure their distance. We have been revisiting this method through a project called “NRT phase-lag distance”. Here we present the method itself and the modus operandi of our project. We also present an analysis of the faint emission in the outer OH maser shell of OH 83.4-0.9 and use this analysis to discuss the limitations of the “phase-lag” method. Finally we compare the distances obtained from this method with those obtained from optical and radio astrometry.

**** European VLBI Network Mini-Symposium and Users’ Meeting (EVN2021) ****
**** 12-14 July, 2021 ****
**** Online ****

PoS(EVN2021)012

---

[*] Speaker

1. Introduction

When an intermediate mass-star (i.e., M $\leq$ 8 $M_\odot$) leaves the Main Sequence it becomes a red giant. It then reaches the Asymptotic Giant Branch (AGB) when the star ceases the core helium burning phase and enters the "double-shell" burning phase. During this stage of their evolution, when the star enters the so-called "thermal pulse phase" (TP-phase) which typically lasts 10^4-10^5 years, the mass-loss rate increases dramatically reaching rates as high as $\dot{M} = 10^{-4}$ $M_\odot$ yr^{-1}. This leads to the creation of a circumstellar envelope (CSE) of dust and gas. Objects with a degenerated CO core such that C/O < 1, often called "O-rich" evolved stars, are consequently able to produce oxygen-bearing molecules in their CSE. Additionally, the conditions in the CSE are such that for three of these oxygen-bearing molecules, maser emission is commonly observed in the radio domain towards evolved stars. SiO masers at 43 GHz are produced in the inner part of the CSE just before the dust formation radius. At intermediate radii, that is roughly from the dust formation radii, H_2O masers at 22 GHz are observed while further out in the outer CSE, OH masers at 1.6 GHz are produced (cf. Fig. 1 presenting a schematic view of the CSE).

Miras, lower(-mass) end stars of the AGB, have modest mass-loss rates and their CSEs are consequently optically thin. As a matter of fact, they have been observed for centuries, like the iconic *o* Ceti (Mira A), and are fervently followed by amateur astronomers, whose observations are used to build their optical lightcurves (e.g. the AAVSO database[1]). From these lightcurves, the pulsating periods of these objects can be inferred and found to be typically in the range of ~100–500 days. At the higher(-mass) end of the AGB, for the objects with the highest mass-loss rate, the amount of dust in the CSE is such that they become optically thick. These so-called "OH/IR" stars are commonly observed and studied through their infrared and OH maser emission. Their periods, inferred from the aforementioned emission, typically range from 1 to 5–6 years.

Evolved stars are present throughout the Galaxy, i.e. in the Galactic disk (including in young stellar clusters, Deguchi et al. 2004), the bulge, and globular clusters in the halo but also in the Magellanic Clouds (Marshall et al. 2004) and their OH maser emission can be used for a wide range of studies (Etoka et al. 2015). In particular, they can provide a direct measure of the velocity fields of these Galactic components. The study of the stellar kinematics in the various Galactic components can be performed via the combination of their radial velocity and luminosity information. Allying their kinematics, age and metallicity information will allow not only to refine Galactic evolution models but also greatly improve our understanding of stellar evolution in different galactic environments. In order to do so though, the determination of the distance of the entire evolved-star population is vital. The OH/IR stage is of short duration due to the high mass-loss rate. It is nonetheless an important stage as it characterises the very tip of the AGB and hence is key to understanding e.g. when and how the pulsation ceases (Engels, Etoka & Gérard 2019) and more generally, how stars transit from this stage to the Planetary-Nebulae phase.

Several methods can be used to infer the distances of evolved stars, such as the Period-Luminosity relation (PLR) observed for Miras, but the relation has been shown not to hold for vari-

---

[1] https://www.aavso.org

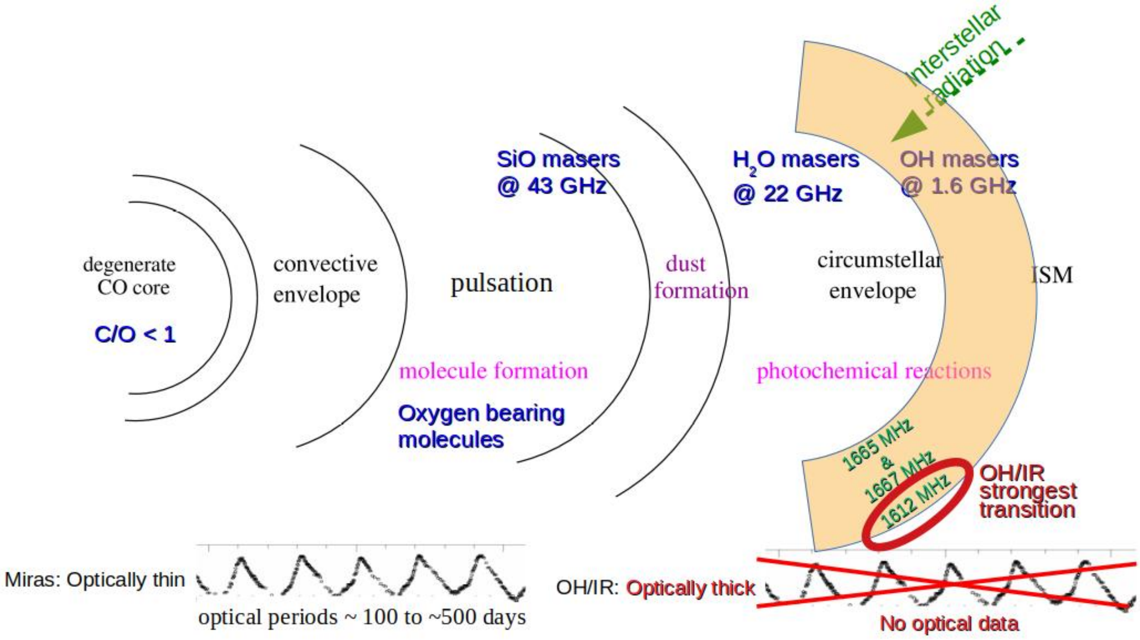

Figure 1: Schematic view of the circumstellar envelope of O-rich evolved stars

able stars with periods longer than ∼ 450 days (Whitelock, Feast & Catchpole 1991). Radio parallax distances have also been successfully obtained for closeby Miras (Vlemmings & van Langevelde 2007) and one OH/IR star (Orosz et al. 2017). But this technique is particularly challenging for OH/IR (even more so for very long-period-variable) stars as it requires the persistence of maser spots over the duration of a whole cycle. Gaia (Gaia Collaboration 2016) will provide a huge step forward in distance determination of the (reasonably) optically-thin fraction of the evolved star population, but it will be of little help for the deeply enshrouded OH/IR stars. The determination of the distance by the phase-lag method circumvents the problems aforementioned. We initiated a project called the “NRT phase-lag distance” to revisit this method and infer the distances of a small sample of OH/IR stars (Engels et al. 2015; Etoka et al. 2018). The method is described in Section 2. Section 3 presents the status of our project using complementary sets of single-dish observations obtained at the Nançay Radiotelescope (NRT) and interferometric maps obtained with either e-MERLIN or the JVLA. Section 4 presents a discussion of the caveats of the method along with a comparison to optical and radio astrometry while conclusive remarks are given in Section 5.

2. Phase-lag Method

The CSE is typically spherical in radial expansion. While Miras can exhibit their strongest OH maser emission in the 1665/1667-MHz mainlines, produced in the more internal and turbulent part of the OH-maser layer where acceleration has not necessarily ended (Etoka & Le Squeren 2004), OH/IR stars produce their strongest maser emission in the 1612-MHz OH ground-state satellite line. The geometrically-thin shell where the 1612-MHz OH maser emission resides is thought to be produced at a distance such that acceleration is no longer present. The velocity distribution of the emission with respect to θ, the angular distance with respect to the central star (hereafter v vs θ distribution), is then simply elliptical (cf. Fig. 2 presenting the schematic view of a standard "thin-"shell model hereafter "standard model") where the emission at the stellar velocity, $v_{\rm star}$, probes the actual angular extent of the shell $\theta_{\rm Sh}$. This emission is characterised by a "double-peak" (often tagged as "double-horn") spectral profile, where the blue- and red-shifted horns emanate respectively from the front and the back caps of the shell. Because of the size of the CSE, it takes days to months for the light to travel it entirely. Long-term single-dish monitoring provides a measurement of the "(phase-)lag" in the variations of the red-shifted emission with respect to the blue-shifted one. The inherent property of the CSE itself can be used to infer the distance of these objects combining the phase-lag, providing a measure of their linear diameter along the line of sight, and interferometric snapshot observations providing a measure of their angular diameter on the plane of the sky (cf. Fig. 3).

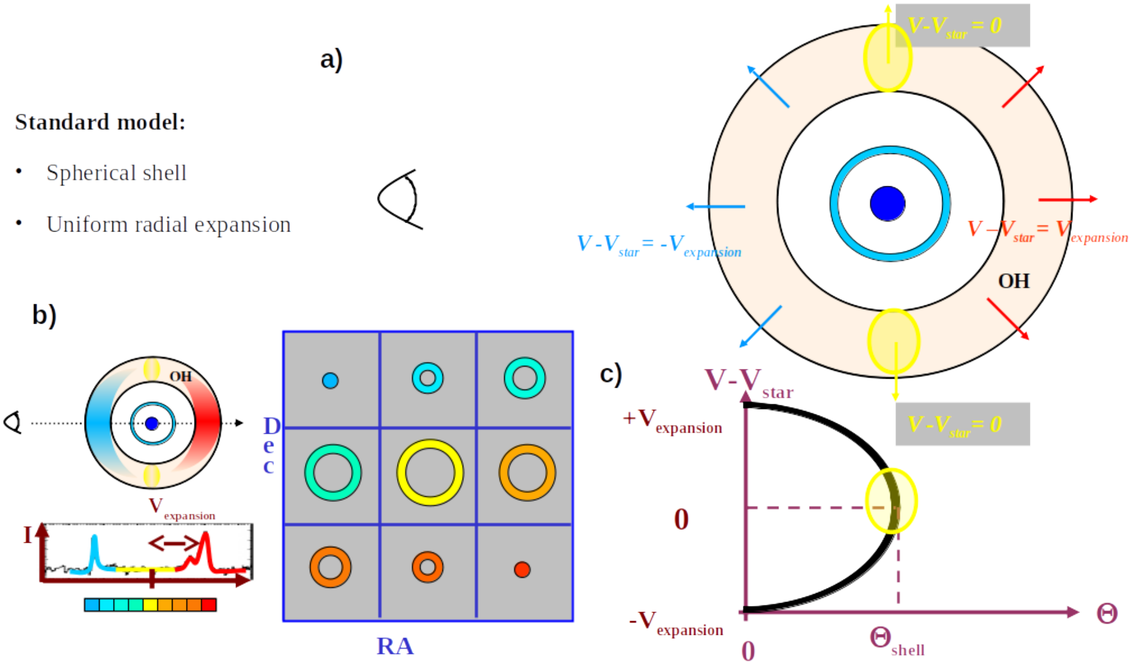

Figure 2: Schematic view of a standard ("thin-")spherical shell expanding in a uniform radial fashion (**a**), which then produces the typical channel map displayed in (**b**), and for which v vs θ distribution is given in (**c**).

The feasibility of phase-lag measurements per se, was first demonstrated by Schultz, Sherwood & Winnberg (1978) thanks to a 2 years monitoring of 12 OH/IR stars. The method was then further explored in a more systematic fashion with the Dwingeloo Telescope towards 33 OH/IR stars (Herman & Habing 1985; van Langevelde et al. 1990). In particular, van Langevelde et al. (1990) propose an analytical method to retrieve the phase lags relying on the 1612-MHz emission to be saturated and the shell compliant with spherical symmetry. The method itself relies on analytical fitting of the light curves.

The modus operandi of the "phase-lag" (τ_0) determination we have implemented for our project relies on simple assumptions. We build the lightcurves of the integrated flux of the blue-shifted and red-shifted emission. We do not rely on any fitting function, instead we assume that the integrated-flux lightcurves of the "blue" and "red" caps of the shell have a similar shape. We then scale and shift the "blue" integrated-flux lightcurve (F_b) with respect to the "red" one (F_r) minimising the

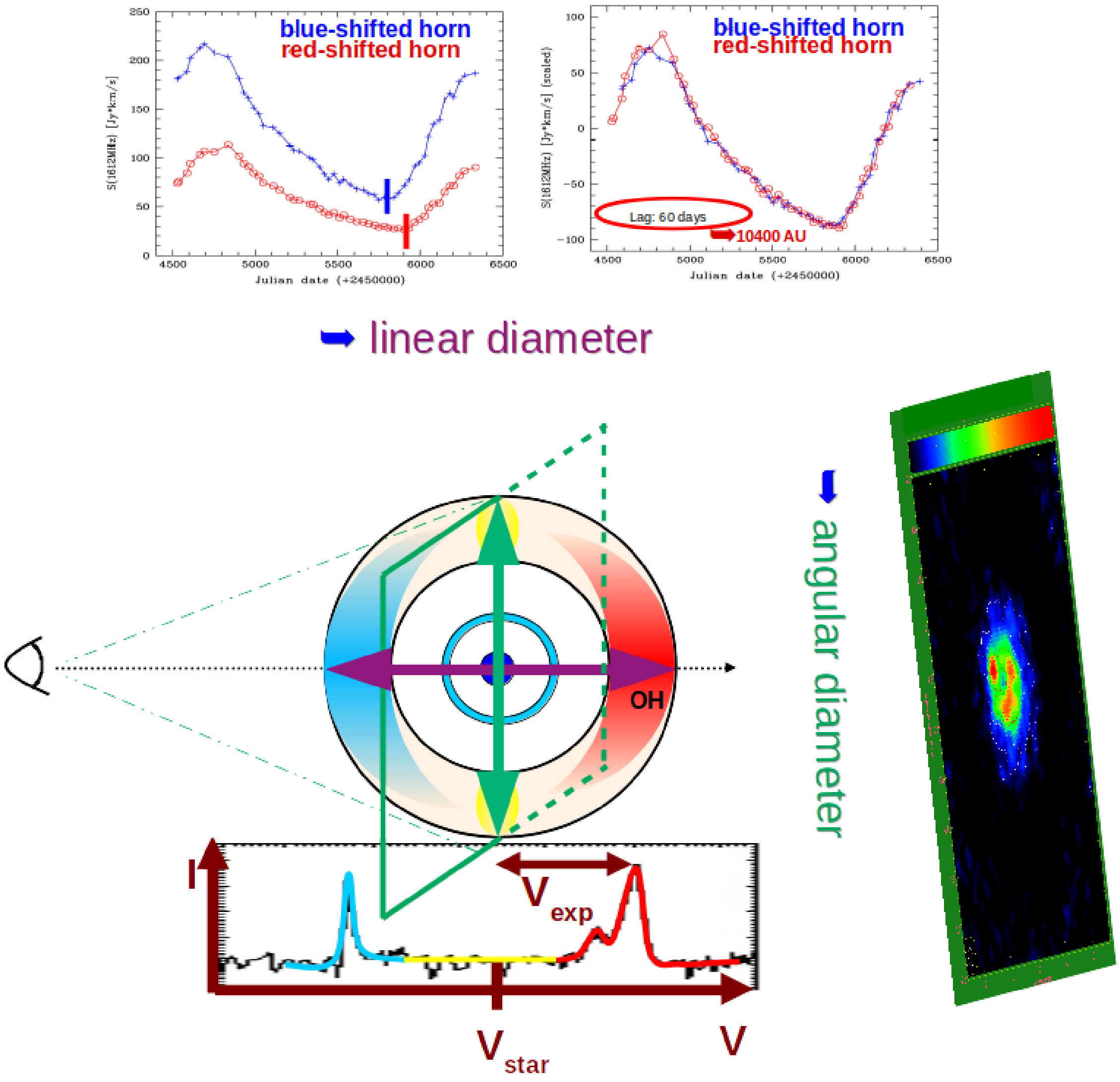

Figure 3: Schematic explanation of the distance determination of an object combining the phase-lag measurement inferred from the single-dish long-term monitoring of its OH emission, leading to the linear diameter determination along the line of sight, and a complementary interferometric observation to infer the angular diameter on the plane of the sky.

function $\Delta F = F_r(t) - a \cdot F_b(t - \tau_0) + c$ (where a and c are constants for the amplitude and mean flux respectively).

In order to infer the angular diameter and hence the distance of the star, a single-epoch high-sensitivity interferometric observation is needed. This single-epoch dataset allows us to check the validity of the "standard model", that is whether the shell complies with spherical geometry, whether it is thin, and whether the outflow velocity is constant within the shell. It also allows us to infer the actual angular extent of the shell, $\theta_{\rm Sh}$, on the plane of the sky as accurately as possible. Because the exact period of an object is never known as there are cycle-to-cycle variations of the length of the period, it is safer to perform its monitoring for at least a complete cycle to ascertain its current variability before performing the interferometric observation.

3. Project observational status

Our phase-lag distance project is composed of 20 sources, which were monitored monthly between 2007 and 2016 with the Nançay Radiotelescope (NRT) down to a sensitivity of 100 mJy with a velocity resolution of 0.035 km s^{-1} so as to obtained several (>2) cycles for each of the objects of the sample. We determined their period (cf. the second column of Table 1 in Section 4) which is also used to infer by extrapolation their next OH maximum/maxima.

Due to the expected size of the objects, for the interferometric mapping of the shell, we have been using e-MERLIN and JVLA, down to a sensitivity of a few ($\leq$ 10) mJy(/beam per channel), making use of our inferred predictions of the maxima to time the observations when the faint interpeak/stellar velocity OH emission is at its strongest.

Figure 4 presents a schematic view of the objects of the project for which we either obtained a high sensitivity map or there exist older low-sensitivity interferometric maps allowing a first estimate or refinement of the distance of the objects (cf. Engels et al. 2015) with the new phase-lag measurements. We also refer to Etoka et al. (2018) for the latest update and preliminary analysis of the overall sample of the project including an estimate of the accuracies achievable in the linear and angular diameter determinations. This leads to uncertainties in the distance, which can reach 20 % for stars with a 1612-MHz maser layer showing deviations from the "standard model".

Beyond obtaining a consistent set of phase-lag measurements, the intent of the project is to obtain high-sensitivity interferometric observations to provide new angular diameters and to improve the determination of angular diameters obtained from lower sensitivity observations in the past. The ultimate aim is to identify the limitations of the method and better constrain the distance uncertainties.

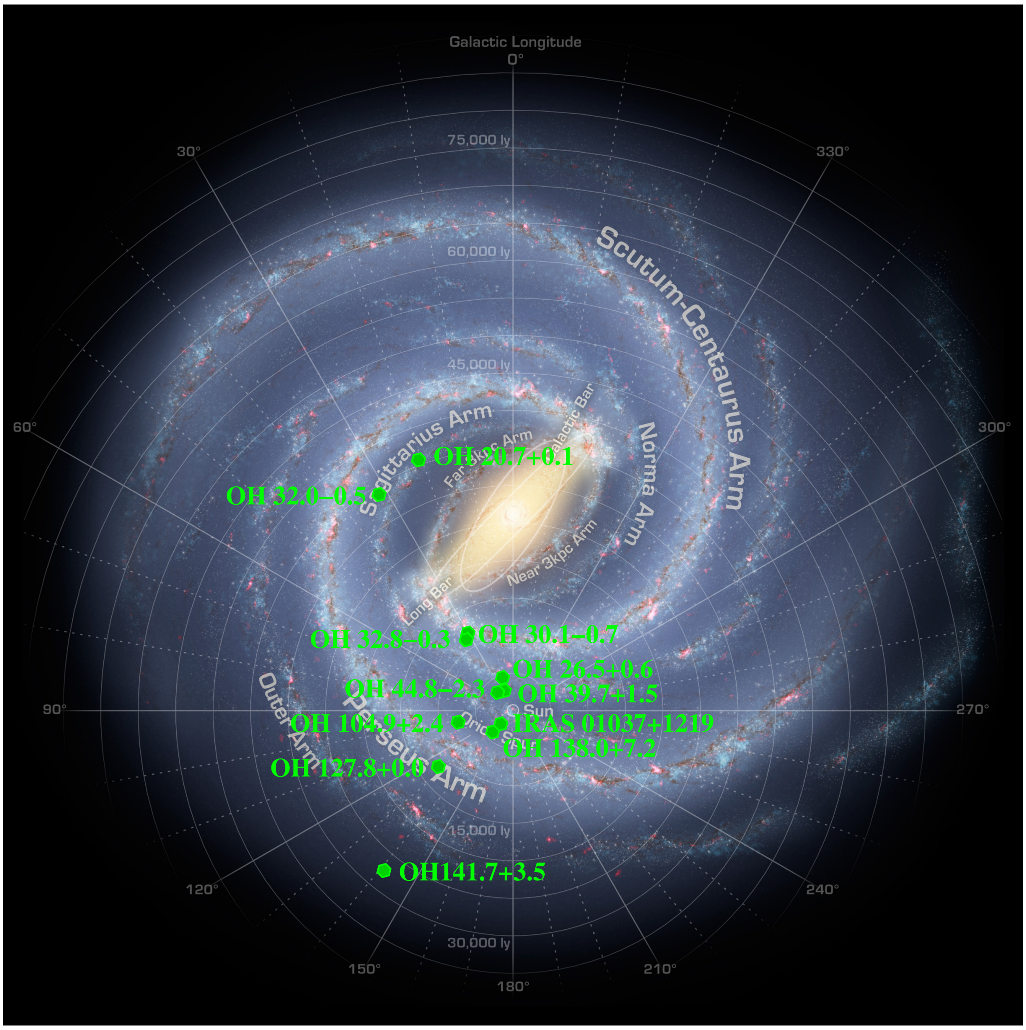

Figure 4: Schematic view of the OH/IR stars of the project for which we could infer a preliminary distance determination from our new NRT phase-lag measurements on the annotated artist's view of the Milky Way (Source: NASA/JPL-Caltech/R. Hurt (SSC/Caltech)).

PoS(EVN2021)012

4. Discussion

4.1 The caveats of the method

Several potential caveats need to be taken into consideration in the distance determination since the method uses two independent measurements of the diameter of the OH maser shell which both have their own specific uncertainties. Additionally, the way these two independent measurements are combined can also introduce an error.

The phase-lag itself depends on the quality of the sampling of the lightcurves, but also of the method used to measure it. If the lightcurves are undersampled (e.g. at the minima and at the maxima of the cycle) this will make the determination of the phase-lag more uncertain. In fact it is actually better to retrieve a regular sampling than retrieving more observations at the minima and maxima themselves while under-sampling the rise and fall to the minima and maxima. The best phase-lag measurement is found to be obtained by using the actual shape of the lightcurves themselves rather than a fit via analytical functions simply because of the complex shape of the lightcurves which can show e.g. additional small "bumps", "plateau-like" minima or maxima etc. This approach assumes implicitly that the "blue" and "red" lightcurves differ only in amplitude(, mean flux) and lag. This is also a safeguard against calibration imperfection such as a poor baseline subtraction of the raw spectra which can bias the phase-lag estimates via an automated algorithm such as the one presented in van Langevelde et al. (1990) as noted by the authors themselves.

As mentioned by van Langevelde et al. (1990), both the geometry and thickness of the shell are important factors when it comes to the accuracy for the distance determination via the phase-lag method. The ideal case is when the 1612-MHz shell fulfils the "standard model" assumptions (cf. Fig. 2), that is the 1612-MHz OH shell is indeed thin and spherical and in uniform radial expansion as in the case of OH/IR star OH 127.8+0.0 (Wolak et al. 2013). In this case the thickness of the 1612-MHz masing shell is negligible which therefore guarantees that the linear diameter, measured along the line of sight can indeed be combined unambiguously with the angular diameter measured on the plane of the sky. For some objects though, deviations from the "standard model" can be observed, as in the case of OH 26.5+0.6 (Etoka & Diamond 2010) with, e.g. clear presence of acceleration still present at the distance of the 1612-MHz maser emission or the shell not fulfilling the "thin-sphericity" requirement for a one-to-one correspondence of the linear and angular diameters.

Even in the case when the thin-spherical-shell requirement is fulfilled, the determination of the actual angular extent of the shell is paramount to a good estimate of the distance. This determination relies unfortunately heavily on the (by nature) very faint interpeak emission near(er) the stellar velocity.

As a general characteristic, the OH masers in the CSE tend to be clumpy (and compact) and well suited for Gaussian fitting. The ideal case for the determination of the angular diameter is to use this characteristic to build the v vs θ distribution of the (Gaussian-fitted) maser components and fit it by an ellipse (cf. Fig. 2). There are two limiting factors nonetheless to this, the first one being the percentage of potentially non-compact emission (for which the Gaussian fitting will not be possible) present in the shell and the second being how much of the outer part of the shell (probed by the interpeak emission) has been detected. For the case of OH 83.4-0.9 observed with e-MERLIN (Etoka et al. 2014), we constructed a high- and a low-spectral-resolution (i.e., 5-channels averaged) dataset to analyse the faint extended emission in more detail. The left-hand side of Fig. 5 presents the spectrum obtained from the e-MERLIN high-spectral-resolution dataset. The top-right panel of Fig. 5 presents the zero-moment map of the entire interpeak emission excluding the strong blue- and red-shifted horns giving a better rendering of the shell structure and extent. The bottom-right panel of Fig. 5 presents the zero-moment map of an even narrower velocity range surrounding $v_{\rm star}$ to highlight the faint emission and its nature. Based on these maps, the actual angular extent of the shell $\theta_{\rm Sh} \geq 1.6$" (Etoka et al. 2014) can be inferred from the faint emission retrieved. It is clear also from the faint-emission-only zero-moment map, that this outer layer is composed for the most part of diffuse maser emission. This latter fact is further confirmed by Fig. 6 which presents on the left the distribution of the compact maser components produced from the high-spectral-resolution dataset and on the right the corresponding v vs θ distribution where the actual extent of the shell, θ_{Sh}, is also shown, further refined by this distribution. This is done by using the minimal extent of the shell inferred from the (convolved) faint emission measurement as a starting guess to find the tightest θ encompassing all the components following the uniform radial expansion criteria, leading to θ_{Sh} ~1.8" (Etoka et al. *in prep.*). The v vs θ distribution constrains rather well the actual thickness/thinness of the shell at the expense of the actual angular extent which is poorly constrained. This shows the importance of the faint emission to constrain this parameter. Note that the isolated North-East "blue" component sitting exactly at θ_{Sh} is purely coincidental as this particular component traces a motion not following the uniform radial expansion of the rest of the shell as clearly visible in the v vs θ distribution.

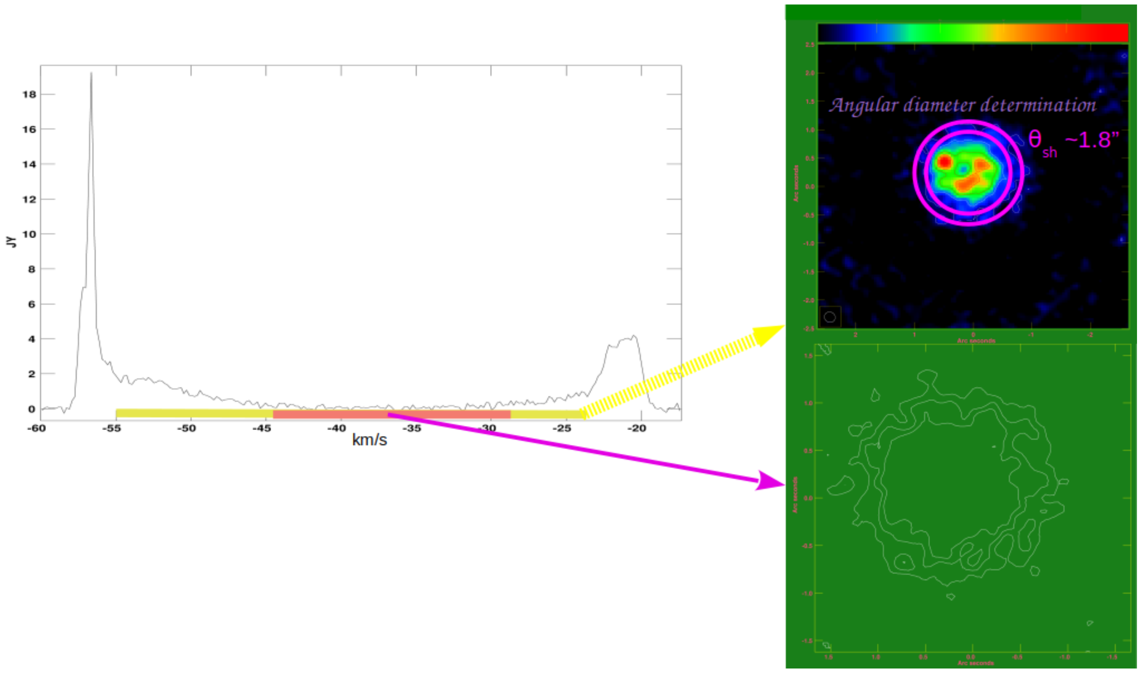

Figure 5: Left: Spectrum obtained from the e-MERLIN high-spectral-resolution dataset where the velocity ranges of the zero-moment maps presented in the right-hand side are given: in yellow for the top-right map, in magenta for the bottom-right map. Top right: Zero-moment map of the entire interpeak emission of OH 83.4−0.9. The outer and inner circles represent the (convolved) size of the diameter of the shell which leads to a deconvolved estimate of θ_{Sh} ~1.8". Bottom right: Zero-moment map of the much restrained velocity-range around v_{star} highlighting exclusively the very faint and mostly "diffuse" emission representative of the actual angular extent of the shell.

Figure 7 shows the similar exercise but this time with the low-spectral-resolution dataset so as to boost the signal to noise. Now the distribution, because of the wide channel width, constrains less well the shell thickness but the distribution explores the shell a bit further out even if it cannot still constrain fully the crucial region of θ around v_{star}.

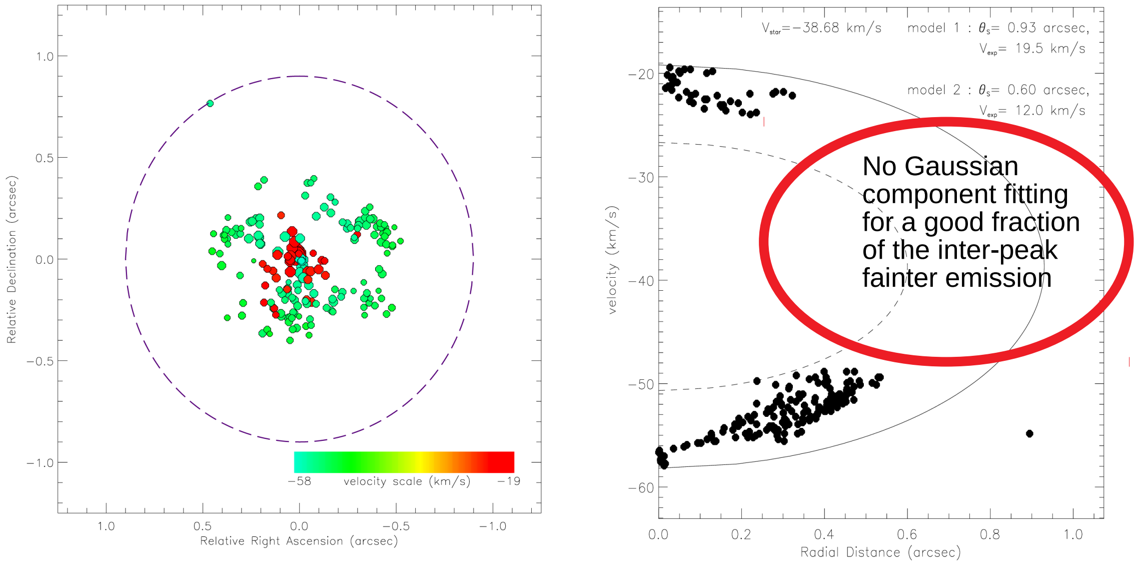

No Gaussian component fitting for a good fraction of the inter-peak fainter emission

Figure 6: Left: distribution of the (Gaussian-fitted) compact maser components obtained from the high-spectral-resolution dataset with the actual angular extent of the shell (the dashed circle) also shown. Right: v vs θ distribution of these (Gaussian-fitted) compact maser components. The outer ellipse is the best model of the outer boundary of the shell. It encompasses all the components following the uniform radial expansion criteria and its radius is constrained by the faint emission (cf. Fig. 5). The inner ellipse is the best fit of the inner maser-layer boundary.

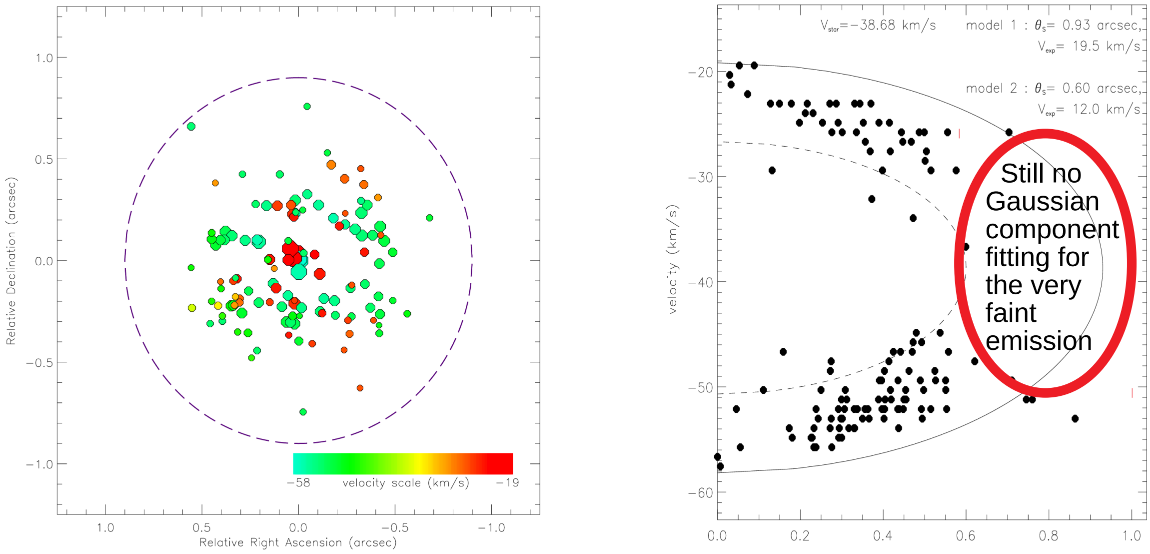

Still no Gaussian component fitting for the very faint emission

Figure 7: Distribution of the (Gaussian-fitted) compact maser components from the low-spectral-resolution dataset (left) & their v vs θ distribution (right) as in Fig. 6. The maser shell boundaries are those determined from the high-spectral-resolution dataset shown in Fig. 6.

In other words, the actual angular diameter is actually better constrained by a direct measurement of the diffuse emission from the zero-moment map directly.

4.2 Comparisons to optical and radio astrometry

To constrain the limitations of the phase-lag method, a comparison with other methods to determine distances could help. Classical methods are the use of the Period-Luminosity-Relation for Mira variables or the use of the radial velocities of the stars together with a model of galactic rotation (kinematic distances). New advances in VLBI and optical astrometry promise to provide distances with higher precision than the classical methods (cf. van Langevelde et al. 2018). In Table 1 we list all objects from the phase-lag sample together with their periods P and phase-lag distances D_{plag} as given by Engels et al. (2015). The latter are compared with kinematic distances and distances derived from Gaia parallaxes.

The applicability of the PLR for Miras, which has been determined in the Large Magellanic Cloud, to galactic Mira variables has been studied by Nakagawa et al. (2016) and Urago et al. (2020) using VERA radio astrometry. The luminosities derived with VERA distances do not contradict the PLR, but the period range probed is small ($350 < P < 450$ days). However, the VERA luminosities of individual stars can deviate substantially from the prediction by the PLR. The phase-lag sample as given in Table 1 has only one star (IRAS 20234–1357) with a period $P < 450$ and a phase-lag distance is not yet available.

Table 1: Comparison of distances derived by various methods for the phase-lag sample.

Object	P [yrs]	D_{plag} [kpc]	D_{kin} [kpc]	D_{Gaia} [kpc]	G$_{RP}$ [mag]	Remarks
IRAS 20234−1357	1.16			0.41±0.03	9.82	
OH 44.8−2.3	1.47	1.0	18.4	1.1±0.7	15.12	
IRC +50137	1.74				14.31	
IRAS 01037+1219	1.78	0.5			14.18	
IRAS 05131+4530	2.88					
OH 39.7+1.5	3.45	0.7	1.3		18.74	
OH 55.0+0.7	3.48		2.3			
IRAS 21554+6204	3.51		1.9			
OH 138.0+7.2	3.86	2.2	2.7			
OH 83.4−0.9	4.11	~3.0	6.1	1.2±0.8	17.46	
OH 32.0−0.5	4.16	10.6	4.3			D_{kin}(far) = 9.7 kpc
OH 127.8+0.0	4.36	3.6	4.1			
OH 26.5+0.6	4.36	1.4	1.9			
OH 75.3−1.8	4.52		4.3			
OH 32.8−0.3	4.63	3.8	3.6			
OH 20.7+0.1	4.71	9.4	6.6			D_{kin}(far) = 9.0 kpc
OH 104.9+2.4	4.79	2.1	2.3			
OH 30.1−0.7	5.95	3.9	5.4			D_{kin}(far) = 9.0 kpc
OH 16.1−0.3	6.03	4.2	1.9	4.5±4.3	13.90	
OH 141.7+3.5	6.05	17.1:	5.4	14.8±74.9	18.80	

Kinematic distances D_{kin} (Table 1) were obtained from the 'Revised kinematic distance calculator (2014)'[2] of the BeSSeL Survey (Reid et al. 2014). We opt for the near kinematic distance if two solutions are possible. If the far kinematic distance is also plausible, we note this distance in the 'Remarks' column. Comparing phase-lag and kinematic distances, incompatibilities were found for OH 44.8–2.3 and OH 141.7+3.5. For the latter object the phase-lag distance is questionable, while for OH 44.8–2.3 the discrepancy is caused by a radial velocity ($v = -71$ km s^{-1}) deviating from expected velocities ($v > 0$ km s^{-1}) in the solar vicinity due to galactic rotation. Using the far kinematic distances for OH 32.0–0.5 and OH 20.7+0.1, the agreement is better than 1 kpc for the remaining objects, except for OH 16.1–0.3, OH 30.1–0.7, and OH 83.4–0.9. The cause for discrepancies between phase-lag and kinematic distances, do not necessarily cast doubt on the phase-lag distances, but could also be due to peculiar movements of the stars on top of the galactic rotation as evident for OH 44.8–2.3.

Orosz et al. (2017) have made radio astrometry of two OH/IR stars, which are part also of the phase-lag sample. For IRAS 01037+1219, they give a lower limit distance estimate of ≥190 pc, which is in accordance with the 500 pc phase-lag distance (see Table 1). In the case of OH 138.0+7.2 they obtained a distance D = $1.9^{+0.4}_{-0.3}$ kpc, which compares well with the phase-lag distance of D_{plag} = 2.2 kpc.

The comparison with distances derived from optical astrometry is limited to stars which are optically not too faint. The strong circumstellar extinction by the dust shells surrounding OH/IR stars often inhibit their detection by optical surveys. This affects in particular the current Gaia astrometry mission (Gaia Collaboration 2016), which is going to provide parallaxes for well above 1 billion stars in the Galaxy. Recent cross-identifications of AGB samples showing SiO (Quiroga-Nuñez et al. 2020) and/or OH maser emission (López Martí et al., in prep.) found detection rates in the Gaia DR2 and EDR3 releases of only 33-40 %.

Table 1 lists the Gaia optical G_{RP} brightnesses in the wavelength range 640 – 1000 nm for the eight stars detected from our sample. They show a broad brightness distribution with a range $\sim 10 < G_{RP} < 19$ magnitude. For five stars, distances D_{Gaia} (with 1σ errors) are available from Bailer-Jones et al. (2021) that are based on the parallaxes provided by the Gaia EDR3 release (Gaia Collaboration 2021). Only for one star, IRAS 20234−1357, the error is smaller than 30 %. IRAS 20234−1357 is the optically brightest OH/IR star and has the shortest period. With P = 423 days, it has the characteristics of a Mira variable. Its distance is $D_{Gaia} = 414 \pm 29$ pc. Unfortunately no phase-lag distance is available so far.

For OH 44.8–2.3 and OH 16.1–0.3, a good agreement is found between the phase-lag and Gaia distance inference. For OH 83.4–0.9, the agreement is poor with the phase-lag distance a factor ~2.5 larger than the Gaia distance. However, because of the relatively large uncertainties of the Gaia parallaxes, the comparisons between the phase-lag and the Gaia distances for these three OH/IR stars are of limited significance. And again: a discrepancy between phase-lag and

---

[2] http://bessel.vlbi-astrometry.org/revised_kd_2014

Gaia distances may not necessarily be due to unrecognised caveats of the phase-lag method. Gaia parallaxes and hence distances also could be compromised, if activity in the stellar photosphere leads to movements of the photocenter on the Gaia images unrelated to the parallax (Chiavassa et al. 2018). This effect was used by Matsuno et al. (2020) to explain the 240 % difference of the parallaxes determined by VERA and Gaia DR2 for the star BX Cam, and may limit the use of Gaia parallaxes to probe the reliability of the phase-lag method.

5. Conclusion

We have presented the distance determination to obscured evolved stars via the “phase-lag” method along with the modus operandi we use in our project to infer distances and the caveats we have identified so far of this method in distance inference.

In terms of the “phase-lag” measurements themselves, we have identified two major caveats: the first one being the quality of the (sampling of) lightcurves and the second being the use of fitting functions. Poorly sampled lightcurves at the maxima and or minima renders the lag measurement rather uncertain and, the complexity of the lightcurves is such that relying on their shape rather than fitting functions is also a better practice to infer the lag with the highest accuracy.

In terms of the angular diameter determinations, the sensitivity of the interferometric observations such that as much as the faint interpeak emission is detected is crucial. Beyond the strength of this emission, for OH/IR sources, it can be mostly of diffuse nature and hence eludes Gaussian fitting. Combining both the zero-moment information of the faint emission with the v vs θ distribution obtained from the compact masers (at a high enough spectral resolution) provides a much greater accuracy of the outer boundaries of the maser shell.

Another major caveat is a possible deviation from the standard thin-shell model either in terms of e.g. geometry of the shell itself (i.e., deviation from sphericity) or thinness of the (maser) layer which can both introduce an additional uncertainty because of the now more complex relation between the (line-of-sight) linear diameter and (plane-of-the-sky) angular diameter measurements. We expect therefore that uncertainties of phase-lag distances cannot be achieved on a $<$ 10 % accuracy with the main limiting factor being the actual/intrinsic thickness of the (maser) layer.

We further analysed the optical and radio astrometry methods at hand to determine distances of AGB stars in the Galaxy (and potentially beyond) as all these methods have their own caveats and should be regarded as complementary. Indeed, in order to constrain stellar evolution itself but also use the evolved-star population to e.g. refine Galactic evolution models, the retrieval of the distances of the stars in all the evolved-phases they will pass through is vital. We consequently compared these various methods of inferring distances of evolved stars in search of potential systematic differences between them. This analysis is based on the OH/IR stars of our sample that are not totally obscured and for which GAIA measurements are available; the two OH/IR stars we know of (and also part of our sample) for which OH parallax measurements have been successfully made and the kinematic distance inferences of the sources of our project. The comparison of these methods has shown no evidence for systematic differences between phase-lag and kinematic and Gaia distances.

Acknowledgments

The Nançay Radio Observatory is the Unité Scientifique de Nançay of the Observatoire de Paris, associated with the CNRS. The Nançay Observatory acknowledges the financial support of the Région Centre in France. e-MERLIN is a UK national facility operated by the University of Manchester at Jodrell Bank Observatory on behalf of STFC.

References

[1] Bailer-Jones C. A. L., Rybizki J., Fouesneau M., Demleitner M., Andrae R., 2021, AJ 161, 147

[2] Chiavassa A., Freytag B., Schultheis M., 2018, A&A 617, L1

[3] Deguchi S., Fujii T., Glass, I. et al., 2004, PASJ, 56, 765

[4] Engels D., Etoka S., Gérard E., 2019, IAUS 343, 389

[5] Engels D., Etoka S., Gérard E., Richards A.M.S., 2015, ASPC 497, 473

[6] Etoka S., Engels D., Gérard E., Richards A.M.S., 2018, IAUS 336, 381

[7] Etoka S., Engels D., Imai I., Dawson J., Ellingsen S., Sjouwerman L., van Langevelde H., 2015, Proc. of "Advancing Astrophysics with the Square Kilometre Array", PoS(AASKA14)125,

[8] Etoka S., Engels D., Gérard E., Richards A.M.S., 2014, PoS(EVN2014)59

[9] Etoka S. & Diamond P.J., 2010, MNRAS 406, 2218

[10] Etoka S. & Le Squeren A.M., 2004, A&A 420, 217

[11] Gaia Collaboration, Prusti T., de Bruijne J. H. J. et al., 2016, A&A 595, A1

[12] Gaia Collaboration, Brown A.G.A., Vallenari A., et al., 2021, A&A 649, A1

[13] Herman J., Habing H.J., 1985, A&AS 59, 523

[14] Marshall J.R., van Loon J.T., Matsuura M. et al., 2004, MNRAS 355, 1348

[15] Matsuno M., Nakagawa A., Morita A., Kurayama T., Omodaka T., Nagayama T., Honma M., Shibata K.M., Ueno Y., Jike T., Yoshiaki T., 2020, PASJ 72, 56

[16] Nakagawa A., Kurayama T., Matsui M., Omodaka T., Honma M., Shibata K.M., Sato K., Jike T., 2016, PASJ 68, 78

[17] Orosz G., Imai H., Dodson R., Rioja M.J., Frey S., Burns R.A., Etoka S., Nakagawa A., Nakanishi H., Asaki Y., Goldman S.R., Tafoya D., 2017, AJ 153, 119

[18] Quiroga-Nuñez L.H., van Langevelde H.J., Sjouwerman L.O., Pihlström Y.M., Brown A.G.A., Rich R.M., Stroh M.C., Lewis M.O., Habing H.J., 2020, ApJ 904, 82

[19] Reid M.J., Menten K.M., Brunthaler A., Zheng X.W., Dame T.M., Xu Y., Wu Y., Zhang B., Sanna A., Sato M., Hachisuka K., Choi Y.K., Immer K., Moscadelli L., Rygl K.L.J., Bartkiewicz A., 2014, ApJ 783, 130

[20] Schultz G.V., Sherwood W.A., Winnberg A., 1978, A&A 63, L5

[21] Urago R., Yamaguchi R., Omodaka T., Nagayama T., Chibueze J. O., Fujimoto M.Y., Nagayama T., Nakagawa A., Ueno Y., Kawabata M., Nakaoka T., Takagi K., Yamanaka M., Kawabata K., 2020, PASJ 72, 57

[22] van Langevelde H.J., Quiroga-Nuñez L. H., Vlemmings W., Loinard L., Honma M., Nakagawa A., Immer K., Burns R., Pihlström Y., Sjouwerman L., Rich R.M., Natarajan I., Deane R., 2018, PoS(EVN2018)43

[23] van Langevelde H.J., van der Heiden R., van Schooneveld C., 1990, A&A 239, 193

[24] Vlemmings W.H.T. & van Langevelde H.J., 2007, A&A 472, 547

[25] Wolak P., Szymczak M., Gérard E., 2013, MNRAS 430, 2499

[26] Whitelock P., Feast, M., Catchpole R., 1991, MNRAS 248, 276